JGR Atmospheres

RESEARCH ARTICLE
10.1029/2020JD033589

# Influence of Thermodynamic State Changes on Surface Cloud Radiative Forcing in the Arctic: A Comparison of Two Approaches Using Data From AFLUX and SHEBA

**Johannes Stapf[1], André Ehrlich[1], and Manfred Wendisch[1]**

[1]Leipzig Institute for Meteorology (LIM), University of Leipzig, Germany

**Key Points:**

- Different approaches to derive the surface cloud radiative forcing (CRF) are compared using data of a case study of the AFLUX campaign
- Radiative transfer-based approaches provide a systematically stronger warming effect of clouds than observed
- For Surface Heat Budget of the Arctic Ocean, atmospheric thermodynamic state changes and profile properties are identified as decisive for the respective annual cycle of longwave CRF

**Correspondence to:**
J. Stapf,
johannes.stapf@uni-leipzig.de

**Citation:**
Stapf, J., Ehrlich, A., & Wendisch, M. (2021). Influence of thermodynamic state changes on surface cloud radiative forcing in the Arctic: a comparison of two approaches using data from AFLUX and SHEBA. *Journal of Geophysical Research: Atmospheres*, *126*, e2020JD033589. https://doi.org/10.1029/2020JD033589

Received 24 JUL 2020
Accepted 29 JAN 2021



**Abstract** The cloud radiative forcing (CRF) quantifies the warming or cooling effects of clouds. To derive the CRF, reference values of net (downward minus upward) irradiances in cloud-free conditions are required. There are two groups of techniques to estimate these reference values; one is based on radiative transfer modeling, and a second group uses measurements in cloud-free situations. To compare both approaches, we first look at a case study from the airborne measurements of radiative and turbulent FLUXes of energy and momentum in the Arctic boundary layer (AFLUX) campaign, where a moving cloud field with a sharp edge separating a cloudy boundary layer from an adjacent evolving cloud-free area was probed. These data enabled the quantification of the impact of changing atmospheric and surface properties relevant for the reference net irradiances in cloud-free conditions. The systematically higher surface albedo below clouds compared to cloud-free conditions, results in a 11 $W \cdot m^{-2}$ smaller shortwave cooling effect by clouds estimated from the radiative transfer approach compared to the measurement-based one. Due to the transition of thermodynamic parameters between the cloudy and cloud-free atmospheric states, a 20 $W \cdot m^{-2}$ stronger warming effect is estimated by the radiative transfer approach. In a second step, radiative transfer simulations based on radiosoundings from the Surface Heat Budget of the Arctic Ocean campaign are used to quantify the impact of the vertical profiles of thermodynamic properties on the CRF. The largest difference between the longwave CRF estimated by the two methods is found in autumn with up to 25 $W \cdot m^{-2}$.

## 1. Introduction

Clouds significantly influence the local surface energy budget in the Arctic. Long-term observations in the Arctic clearly demonstrated the close link between synoptically driven atmospheric and radiative states (Graham et al., 2017; Miller et al., 2017; Stramler et al., 2011; Walden et al., 2017). Large scale processes, which can force changes between these states by advecting warm and moist air masses into the Arctic, may dominate the surface energy budget for several days (Stramler et al., 2011) and directly affect the freezing or melting of the sea ice (Persson et al., 2017; Tjernström et al., 2019). As a function of microphysical and macrophysical properties and prevailing surface and solar insolation conditions, clouds contribute to changes in the surface radiative energy budget (REB) and induce a warming or cooling of the surface (e.g., Dong et al., 2010; Ebell et al., 2020; Miller et al., 2015; Shupe & Intrieri, 2004). A quantitative measure of the warming/cooling effect is defined by the cloud radiative forcing (CRF, $\Delta F$), after Ramanathan et al. (1989):

$$\Delta F = F_{\text{net, all}} - F_{\text{net, cf}}. \quad (1)$$

$\Delta F$ represents the difference between the shortwave (0.2–4 $\mu$m) and/or longwave (4–100 $\mu$m) net (downward minus upward) irradiances ($F_{\text{net}} = F^{\downarrow} - F^{\uparrow}$) in cloudy ($F_{\text{net, all}}$) and cloud-free conditions ($F_{\text{net, cf}}$). For calculating the CRF, the determination of $F_{\text{net, cf}}$ as a reference is decisive. This quantity has to be estimated, because usually the measurements are taken in cloudy conditions.

Stapf et al. (2020a) have discussed two groups of techniques to estimate the reference values of net irradiances in cloud-free conditions: (1) A radiative transfer-based (also called instantaneous) approach uses radiative transfer simulations of the atmospheric/surface state in cloudy conditions without the cloud (removed hydrometeors). (2) In a measurement-based (also called climatological) approach the cloud-free net irradiances are measured during cloud-free periods, which are separated in time and/or space from

the observations in cloudy situations. As both approaches relate net irradiances from a cloudy to a cloud-free atmospheric state, changes in radiation-relevant parameters like the thermodynamic profile or surface properties between these states are crucial.

When a cloud-free atmospheric boundary layer transforms into a cloudy state, the strongly negative (outgoing) longwave net irradiances (loss of radiative energy) at the surface during cloud-free conditions shift upward toward the cloud top, causing an elevated temperature inversion, which is further strengthened by the associated radiative cloud top cooling. Similar thermodynamic state changes are caused by the downward emission of longwave irradiance from the cloud base, enhancing the longwave radiation reaching the ground, relative to cloud-free conditions. This leads to a warming of the surface due to clouds in the longwave wavelength range. Because the transition from the cloud-free to the cloudy atmospheric thermodynamic state takes some time, the temperature increases steadily and the new equilibrium is not reached instantaneously. The new equilibrium is typically established within hours to days (Walsh & Chapman, 1998). As a result of these cloud-related processes, the atmospheric static vertical stability is modified and the turbulent energy and momentum fluxes respond, potentially causing a dissolution of surface-based temperature inversions. These inversions are frequently observed in the Arctic during cloud-free conditions; they are caused by negative (outgoing) longwave net irradiances at the surface in combination with high-pressure systems and related subsidence of air. In addition, advection of warm and moist air masses influence or induce the transformation between the cloudy and cloud-free states (Stramler et al., 2011). These processes may potentially mask the local cloud impact on the surface REB.

In addition to these changes of the thermodynamic state in the Arctic, the solar illumination conditions play a crucial role for the REB by modifying the surface albedo. In a cloudy atmosphere, the shortwave radiation below the clouds is diffuse. Diffuse radiation in cloudy conditions has different spectral characteristics as compared to irradiances in cloud-free conditions, which may increase or decrease the shortwave surface albedo, compared to cloud-free conditions. This influence of clouds depends on the complex interaction of physical surface properties, the solar zenith angle (SZA), and cloud optical thickness (Gardner & Sharp, 2010; Warren, 1982). As shown by Stapf et al. (2020a), these surface albedo modifications due to clouds are of essential importance to estimate the solar cooling effect of Arctic clouds over snow covered sea ice.

Stapf et al. (2020a) quantified a systematic bias for the shortwave radiative transfer-based CRF. However, Stapf et al. (2020a) based their conclusions on radiative transfer simulations, as no closely collocated (temporally and spatially) measurements in cloudy-free and cloudy conditions were available for that study. For the longwave top of atmosphere CRF, Allan and Ringer (2003) quantified inconsistencies between the measurement-based CRF derived from satellite observations and the radiative transfer-based CRF extracted from climate models. The differences are explained by thermodynamic changes, which are considered in the satellite observations (real cloud-free subsamples), but not incorporated into the model approach, where the cloud-free state was simulated by artificially removing the cloud from the atmosphere.

Both approaches to estimate the CRF have been applied in the Arctic. The radiative transfer-based approach was applied by Intrieri et al. (2002), Shupe and Intrieri (2004), and Sedlar et al. (2011), and more recently by a slightly adjusted approach by Miller et al. (2015) and Ebell et al. (2020) using surface albedo observations under cloud-free conditions fitted as function of SZA. The measurement-based approach was employed by Walsh and Chapman (1998), Dong et al. (2010), and Cox et al. (2016). The resulting CRF estimates provided valuable insights on the CRF at different locations and seasons and consequentially have been compared with each other, however, without assuring that they are comparable in quantitative terms. A truly observation-based comparison between the CRF values derived from both approaches covering shortwave and longwave radiative effects, as well as a measurement-based quantification of the influence of the assumed thermodynamic profile properties has not been reported so far.

To close this gap, we present and analyze observations from two campaigns: the airborne measurements of radiative and turbulent FLUXes of energy and momentum in the Arctic boundary layer (AFLUX) campaign, and the Surface Heat Budget of the Arctic Ocean (SHEBA) expedition (Uttal et al., 2002). During

AFLUX we were fortunate enough to observe an atmospheric situation over sea ice with a sharp cloud edge separating a cloudy, potentially coupled boundary layer from an evolving cloud-free atmosphere with a surface-based inversion (Section 2). This specific constellation enabled the direct measurement of the radiative impact of clouds on the surface REB with closely adjacent measurements in cloudy and cloud-free conditions over the same type of surface. This measurement-based estimate of CRF is compared to calculations of the CRF using radiative transfer simulations to estimate the cloud-free net irradiances (pretending no measurements in cloud-free conditions were available) (Section 3). Different factors for the differences found are discussed. Furthermore, to study the related differences in longwave CRF estimates on a longer-term basis and investigate seasonal changes of CRF estimates based on both methods, SHEBA observations are analyzed (Section 4).

## 2. Observations, Case Study, and Approaches

### 2.1. Data Basis and Radiative Transfer Simulations

During March and April 2019, the AFLUX campaign was conducted in the marginal sea ice zone (MIZ) north-west of Svalbard. AFLUX was a follow-up mission to late spring measurements collected during the Arctic CLoud Observations Using airborne measurements during polar Day (ACLOUD) campaign (May/June 2017) introduced by Wendisch et al. (2019). During AFLUX, the Polar 5 research aircraft from the Alfred Wegener Institute Helmholtz Center for Polar and Marine Research (AWI) was used to observe, among other aspects, the Arctic boundary layer during low-level flights in early spring. The REB was quantified using two pairs of broadband pyranometers (0.2–3.6 $\mu$m) and pyrgeometers (4.5–42 $\mu$m) measuring upward and downward shortwave and longwave irradiances collected with a frequency of 20 Hz. The instrumental payload and processing algorithms of the radiation data applied during ACLOUD (Ehrlich et al., 2019) were also operated during AFLUX. Relevant parameters for the CRF and the REB derived from instruments on the aircraft, like surface brightness temperature (BT) (measured by a Kelvin infrared radiation thermometer (KT-19)), sea ice concentration (derived from a digital camera with a hemispherical lens), and in situ observations of the thermodynamic state are introduced in Stapf et al. (2020a). CRF estimates are analyzed for flight altitudes below 100 m at a flight speed of 50–60 m $s^{-1}$ resulting in an horizontal resolution of the REB components of 2.5–3 m. Differences between the CRF and REB derived at flight level and the surface were estimated from radiative transfer modeling of atmospheric profiles used in this study and for the typical flight altitude in low-level sections. Differences are in the range of 1–2 $W{\cdot}m^{-2}$ and, thus, less than measurement errors (Ehrlich et al., 2019; Stapf et al., 2020a). As a consequence, they were neglected in the further analysis.

The radiative transfer simulations of the irradiances for the cloud-free reference are performed with the libRadtran package (Emde et al., 2016) in the configuration described by Stapf et al. (2020a). The required vertical profiles of thermodynamic properties are derived from in situ aircraft measurements of temperature and humidity. They are merged with radiosoundings from Ny-Ålesund (Maturilli, 2020) for altitudes above the maximum flight levels of the aircraft. They are also matched with surface temperatures observed by an infrared thermometer on board of Polar 5 for levels below the lowest flight altitude (50 m).

Important cloud properties were estimated from measurements collected during the low-level flights below clouds. The equivalent liquid water path (LWP) was derived from the shortwave irradiance measurements in combination with radiative-transfer-simulated lookup tables of shortwave broadband transmissivity, which have been produced for the locally observed atmospheric profiles and SZAs as a function of cloud LWP (assuming a cloud droplet effective radius of 8 $\mu$m) and surface albedo (Stapf et al., 2020a).

In Section 4 data obtained during the SHEBA campaign (Uttal et al., 2002) conducted from October 1997 to October 1998 are analyzed, which provided a unique insight in the inner Arctic surface energy budget (Persson et al., 2002) north of Alaska (75°N-80°N). The combination of in situ measurements performed on an ice floe camp and ground based remote sensing of cloud properties, together with atmospheric state observations enabled, among other aspects, the characterization of the impact of clouds on the surface energy budget (Intrieri et al., 2002; Shupe & Intrieri, 2004) and track the seasonal evolution of multiyear sea ice floe properties for the entire year (Perovich et al., 2002).

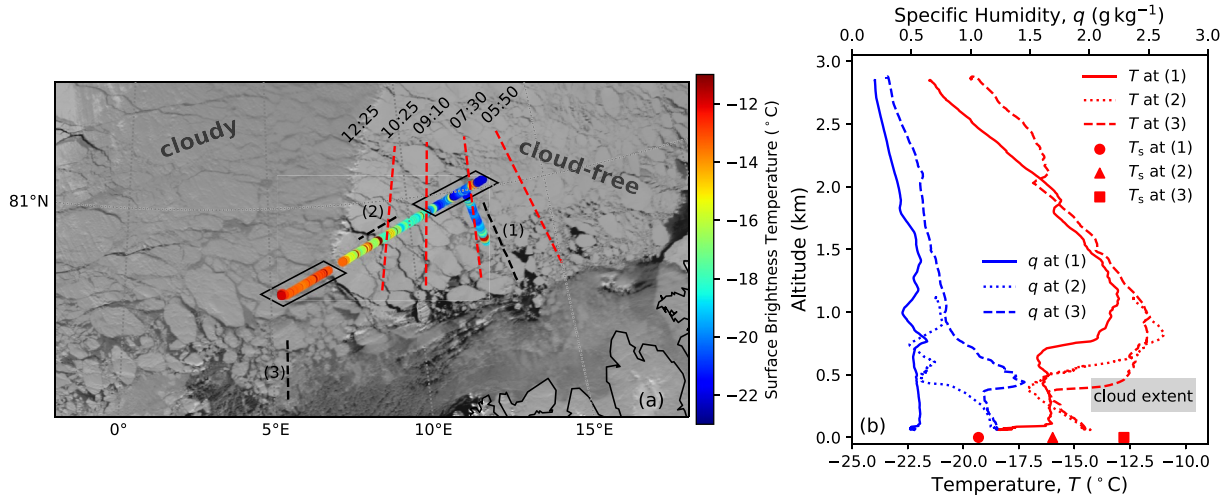


**Figure 1.** (a) MODIS satellite image (12:25 UTC) of a cloud edge observed in the MIZ on April 11, 2019 overlaid with the surface brightness temperature (BT) measured along the flight track (color scale trimmed at −11°C). Red dashed lines indicate the locations of the cloud edge derived from previous satellite images (times in UTC). (b) Measured temperature and specific humidity profiles in the cloud-free east (1), cloudy west (3), and in the center of the flight track (recently cloud-free) (2) are shown with dashed black lines in (a). Remote-sensed surface temperatures ($T_s$) for each profile are shown in red scattered markers. Black boxes in (a) highlight the projected low-level sections used for the comparison in Section 3. Gray box in (b) indicates the maximum observed cloud vertical extents in the cloud field.

### 2.2. Case Study of a Moving Cloud Field Adjacent to an Adapting Cloud-Free Area

On April 11, 2019 a high pressure system was located in the north of Svalbard causing weak easterly winds and large scale subsidence in the region north of Svalbard. In these conditions, a sharp cloud edge evolved, as illustrated by the Moderate Resolution Imaging Spectroradiometer (MODIS) satellite image in Figure 1a at approximately 7°E. In the course of the day, the position of this cloud edge moved from east to west (as indicated by the dashed red lines in Figure 1a). The movement of the cloud field was caused either by advection or dissipation and subsidence; it eventually transformed into cloud-free conditions over the sea ice. Below the cloud layer as well as in the cloud-free area, horizontal low-level flights were performed at an average altitude of 68 m within 1 h, interrupted by vertical profile and stair-case flight patterns to characterize the boundary layer structure and the cloud field. In Figure 1a the surface BT is shown in a color scale; it is obtained from altitudes below 1,200 m within a time period of 1.5 h. The BT instead of surface temperature is presented here to avoid ambiguities caused by the heterogeneous surface types with different surface emissivities. The surface temperature, however, is almost identical to the BT below the cloud field; it is typically 0.5 K warmer in cloud-free conditions as estimated from radiative transfer simulations assuming a surface emissivity of 0.99.

The sea ice conditions (Figure 1a) were characterized by numerous leads and/or nilas (dark and partly covered by snow or frost flowers). Therefore, strong fluctuations of surface temperature and albedo transfer into the upward shortwave and longwave irradiances. Even for snow surfaces, a strong variability in surface roughness caused by pressure ridges and sastrugi significantly influence the observed surface albedo. The variability of surface temperatures below the cloud-field is weaker compared to cloud-free conditions, which might be caused by less strong conductive fluxes below the cloud-field. To avoid a bias in the comparison of estimated CRF values, caused by different sea ice conditions, we focus on snow-covered thick ice flows in the following, which represent the major surface type in this particular case. Therefore, the data were filtered for a surface albedo threshold of 0.77 and sea ice fractions ($I_f$) larger than 95%. These thresholds were defined on the basis of visual surface type classification and the sea ice fraction, which has been derived from fish-eye camera observations. The filter excludes nilas covered by thin snow or frost flowers, which appear slightly darker than thick snow, as well as dark nilas and leads. An estimate of the cloud properties was obtained by the cloud equivalent LWP. For the inner cloud field, a mean/median LWP of 38/36 g·m$^{-2}$ was obtained, representing typical Arctic boundary-layer clouds. The cloud base was located around 200 m while the cloud top and temperature inversion height was more variable between 380 and

480 m with the cloud top slightly above the temperature inversion base. Toward the cloud-edge, the cloud-field appeared thinner and more broken with a vertical extent of approximately 100 m.

At positions (1–3), see Figure 1a, vertical profile flights up to 3 km altitude (1.2 km in the center) were conducted within a time period of 3 h. The resulting temperature and specific humidity data are shown in Figure 1b together with the maximum vertical cloud extent in the cloud field. Additional profiles were flown in between these three profiles to characterize the changing cloud and boundary layer structure, which are not shown for reasons of clarity. In the cloud-free part of the flight track the warming of the surface by the cloud vanishes and the radiative cooling at the cloud top propagates toward the surface. The surface temperature responds to the new surface energy conditions and starts to cool, which decreases the near surface air temperature. However, this adjustment is not instantaneous and may take several hours. The observations of the surface temperature show a decrease by up to 10 K along the entire flight leg. The cooling was observed at locations where up to 5 h earlier the position of the cloud edge was located (red dashed lines in Figure 1a); it is caused by an interplay between the new radiative and turbulent heat fluxes, as well as conductive heat fluxes in the snow-covered ice flows. Due to the temperature decrease at the surface, a surface-based temperature inversion evolves (Figure 1b) from the previously cloudy and potentially coupled profile in the west (Figure 1b, dashed line). The secondary inversion in cloud-free conditions (east) is significantly higher and can be interpreted as the residual cloud top inversion of the dissolved cloud field. This indicates either the influence of large scale subsidence, or advection of a different airmass characterized by a previously higher boundary layer. The cloud-free atmosphere in the vicinity of the cloud edge is characterized by a slightly higher, and thus, a somewhat cooler residual cloud top inversion (Figure 1b, dotted). The specific humidity profiles, however, indicate that the humidity inversion above the cloud top in the west (Figure 1b, blue dashed) is completely absent in the cloud-free atmosphere close to the cloud edge (Figure 1b, blue dotted), while the boundary layer still features similar humidity values. In addition, the atmosphere in cloud-free conditions becomes drier and colder, which affects the downward longwave and shortwave irradiances. Visual impressions during the flight in cloud-free conditions indicated a slightly hazy atmospheric boundary layer.

### 2.3. Two Approaches to Derive the CRF

To quantify the CRF, we apply two common techniques which have been discussed in Stapf et al. (2020a) (their Section 2). The radiative transfer-based approach (subscript "rt") derives the longwave (subscript "lw") CRF ($\Delta F_{\mathrm{lw,rt}}$) by:

$$\Delta F_{\mathrm{lw,rt}} = F_{\mathrm{net,lw,all}} - F_{\mathrm{net,lw,cf}}\Big|_{\mathrm{rt}}, \tag{2}$$

including net irradiances measured in the cloudy (meaning all-sky, subscript "all") atmospheric conditions ($F_{\mathrm{net,lw,all}}$), and the cloud-free reference (subscript "cf," $F_{\mathrm{net,lw,cf}}\big|_{\mathrm{rt}}$) determined by radiative transfer simulations based on observations of thermodynamic atmospheric properties in cloudy conditions (atmospheric profiles of temperature and humidity) without the cloud. This approach does not account for potential surface or atmospheric temperature changes related to the transition between the cloudy and cloud-free state. Therefore, it provides values of CRF similar to the radiative transfer-based cloud radiative effect (CRE) (Cox et al., 2015), which is defined as the difference between cloudy and cloud-free downward irradiances (not net irradiances).

In contrast, the measurement-based approach (subscript "me") involves the net longwave irradiances for the cloud-free reference from observations in cloud-free conditions ($F_{\mathrm{net,lw,cf}}\big|_{\mathrm{me}}$):

$$\Delta F_{\mathrm{lw,me}} = F_{\mathrm{net,lw,all}} - F_{\mathrm{net,lw,cf}}\Big|_{\mathrm{me}}. \tag{3}$$

While the cloud-free reference value for the radiative transfer-based approach is continuously available, for the measurement-based approach observations in the cloudy and cloud-free state are not available at the same time/location. For the AFLUX case study, $F_{\mathrm{net,lw,cf}}\big|_{\mathrm{me}}$ is derived directly from measurements in

the cloud-free adjacent area. In other studies (as discussed in Stapf et al. [2020a]), the irradiances for the required cloud-free reference are obtained by extrapolation, fitting algorithms, or monthly averaged measurements, especially required during longer prevailing cloudy periods.

For the shortwave (subscript "sw") CRF, the consideration of the thermodynamic profile properties and the surface albedo are crucial, which differ in cloudy and cloud-free conditions. As discussed by Stapf et al. (2020a), different concepts have been developed to incorporate the difference between cloud-free and cloudy surface albedo, $\alpha_{cf}$ and $\alpha_{all}$. Here we consider the radiative transfer-based CRF, which uses the surface albedo $\alpha_{all}$ and the thermodynamic profile data, both measured in cloudy conditions, to calculate the net irradiances of the cloud-free reference:

$$F_{\text{net,sw,cf}}\Big|_{\text{rt}} = F^{\downarrow}_{\text{sw,cf}}\Big|_{\text{rt}} - \alpha_{\text{all}} \cdot F^{\downarrow}_{\text{sw,cf}}\Big|_{\text{rt}}. \tag{4}$$

The measurement-based shortwave CRF is based on measurements in the cloud-free state, and consequently includes the $\alpha_{cf}$ as well as the observed irradiances of the cloud-free conditions.

Additionally, we present a modified approach to estimate the radiative transfer-based shortwave CRF based on a cloud-free surface albedo retrieval (Stapf et al., 2020a). Thereby, $\alpha_{all}$ in Equation 4 can be replace by an estimated cloud-free albedo $\alpha_{cf,\,ret}$, which can be retrieved (subscript "ret") from observations under cloudy conditions. Such improved shortwave radiative transfer-based CRF estimates are also found in more recent studies (Ebell et al., 2020; Miller et al., 2015), applying different methods to obtain the cloud-free albedo.

## 3. CRF Case Study During AFLUX

The cloud field and the adjacent cloud-free area observed on April 11, 2019 (Section 2.2) provided a unique opportunity to follow in detail changes in the boundary layer properties caused by the transition from the cloudy to the cloud-free states, and thus, to directly observe the impact of the cloud field on the REB, avoiding the need of radiative transfer simulations. All irradiances needed to derive the CRF have been measured. The closely collocated (spatial and temporal) observations of both the cloudy and cloud-free states strictly relate to the original definition of CRF after Ramanathan et al. (1989). Thus, this data set allows the evaluation of the dependence of CRF estimates on the different approaches and quantify the influence of changing atmospheric thermodynamic and surface properties on the reference cloud-free net irradiances (Sections 3.1 and 3.2) and eventually on the CRF (Section 3.3) obtained by both approaches.

### 3.1. Surface Albedo

The surface albedo represents an important component of the shortwave REB. The airborne observations during the presented case study provide the rare opportunity to appropriately compare the surface albedo of snow-covered sea ice in cloudy ($\alpha_{all}$) and cloud-free ($\alpha_{cf}$) conditions for an almost constant SZA. The surface albedo (filtered for snow covered ice flows) observed below clouds and in cloud-free conditions is shown in Figure 2a, further average values of parameters relevant for the CRF observed in both conditions are given in Table 1. The mean surface albedo below clouds ($\alpha_{all} = 0.874$) is higher compared to the surface albedo in cloud-free conditions ($\alpha_{cf} = 0.842$). Such a difference is in the expected range estimated from radiative transfer modeling for similar SZA values, cloud optical thickness, and fresh snow (Gardner & Sharp, 2010).

The surface albedo difference between cloudy and cloud-free states is supposed to be a primary source for differences between the values of the shortwave CRF obtained by the two common approaches. To correct the surface albedo-induced CRF differences, the albedo parameterization by Gardner and Sharp (2010) was applied to describe the surface albedo under cloud-free conditions on the basis of the observations below clouds ($\alpha_{cf,\,ret}$) as shown by Stapf et al. (2020a). The parameterization was used to generate lookup tables of surface albedo as a function of the SZA, the snow grain size, and the cloud optical thickness. The unknown impurity load of absorbing carbon within the snow was fixed to 0.1 ppmw. Isolines of snow grain size together with the observed surface albedo in cloud conditions and the cloud LWP obtained from

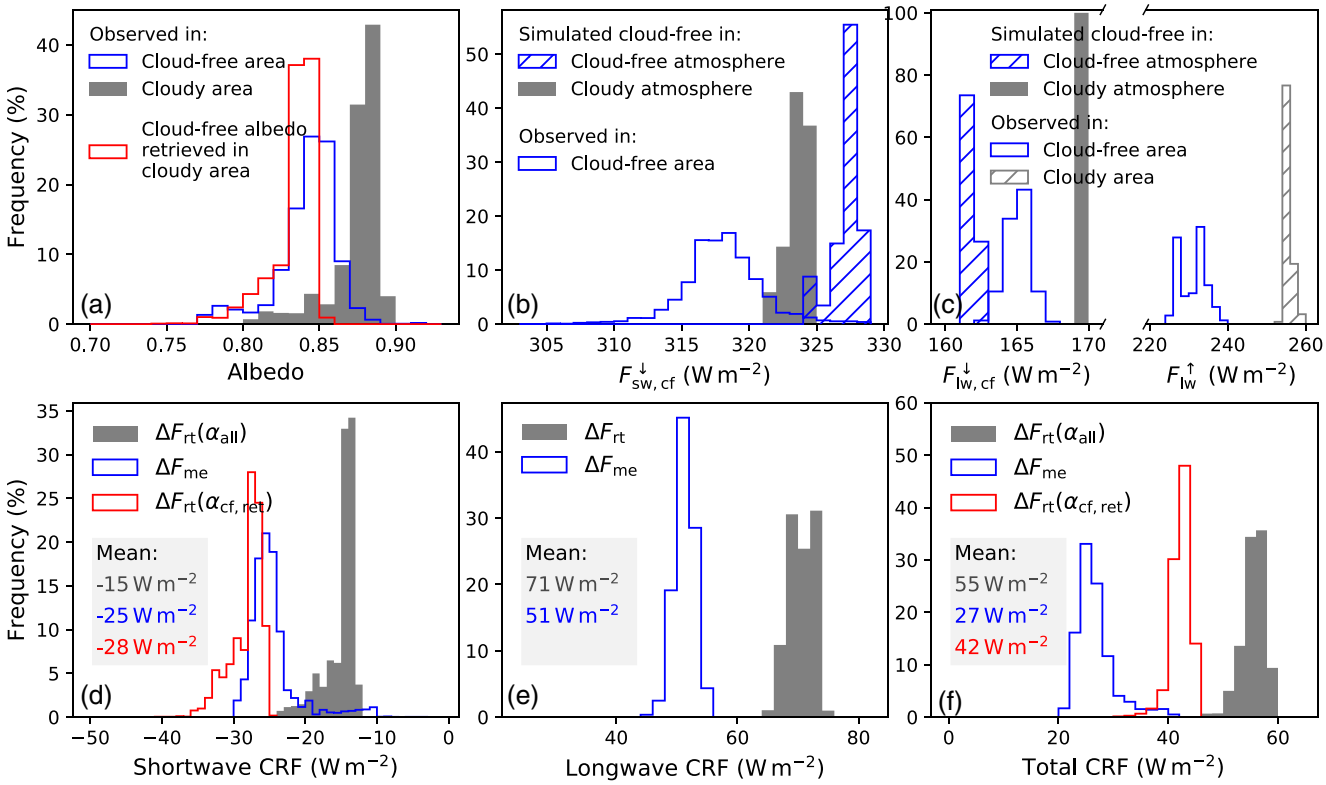


**Figure 2.** Frequency distribution of (a) observed and retrieved surface albedo, (b) observed and simulated cloud-free downward shortwave, (c) downward and upward longwave irradiances in the specific area as indicated in the legend. Simulations are performed with the specific atmospheric thermodynamic profile described in the legend (without a cloud). (d) Shortwave, (e) longwave, and (f) total cloud radiative forcing (CRF) derived using different approaches along the analyzed flight section in the cloudy area. The mean CRF values are given in the embedded text boxes.

the transmissivity-based retrieval are used to extrapolate the cloud-free albedo following the procedure described by Stapf et al. (2020a) (their Figure 8). This enables calculations of the radiative transfer-based shortwave CRF using an appropriate estimated cloud-free surface albedo. The retrieved cloud-free surface albedo ($\alpha_{cf,\,ret}$) in the cloudy area is shown in Figure 2a (red). The mean value of 0.833 obtained by the retrieved cloud-free albedo estimate roughly agrees with the mean surface albedo observed in the cloud-free area (Table 1).

Despite the filtering, both distributions indicate a strong variability of the surface conditions during each of the 30 km long flight legs, which were potentially caused by a variable snow grain size, snow thickness, and surface roughness like sastrugi and pressure ridges. Due to the large horizontal distance between both

**Table 1**
*Observed Components of the REB in W·m$^{-2}$ in Cloud-Free and Cloudy Area of the April 11, 2019 AFLUX Case Study (Boxes in 1)*

| | Observations | | | | | | | | Simulated cloud-free | | Retrieved |
|---|---|---|---|---|---|---|---|---|---|---|---|
| Area | $F^{\downarrow}_{lw}$ | $F^{\uparrow}_{lw}$ | $T_s$ | $F_{net,\,lw}$ | $F^{\downarrow}_{sw}$ | $\alpha$ | $F_{net,\,sw}$ | $F_{net}$ | $F^{\downarrow}_{lw,cf}$ | $F^{\downarrow}_{sw,cf}$ | $\alpha_{cf,\,ret}$ |
| Cloud-free | 165 | 231 | −20 | −66 | 318 | 0.842 | 50 | −16 | 162 | 327 | 0.845 |
| Cloudy | 241 | 255 | −13 | −15 | 204 | 0.874 | 26 | 11 | 170 | 324 | 0.833 |

*Note*. Surface temperature $T_s$ is given in °C; albedo without unity. Simulated components of the cloud-free reference ($F^{\downarrow}_{lw,cf}$, $F^{\downarrow}_{sw,cf}$) are simulated using the thermodynamic profile of the cloudy or cloud-free atmosphere without a cloud. The cloud-free albedo retrieval ($\alpha_{cf,\,ret}$) is applied in both conditions.

flight legs, approximately 90 km, also regional differences potentially may have affected the local conditions and this comparison.

### 3.2. Downward and Upward Irradiances for the Cloud-Free Reference

#### 3.2.1. Shortwave

The next component of the shortwave cloud-free net irradiance is the downward irradiance, which is affected by the surface albedo due to multiple scattering between surface and atmosphere, the absorption by atmospheric gases, in particular water vapor, and the scattering/absorption due to aerosol particles. These processes might change between the transition from the cloudy to the cloud-free states, and thus, influence the obtained cloud-free reference irradiances from both approaches.

In Figure 2b, the observed $F^{\downarrow}_{\mathrm{sw,cf}}$ in the cloud-free area (blue) is compared to the simulated one assuming cloudy (gray) or cloud-free (blue hatched) thermodynamic atmospheric profiles (always without a cloud). Due to the time, which elapsed during the analyzed flight legs, the SZA (around 72°) changed by approximately 0.5° causing a 9 $\mathrm{W{\cdot}m^{-2}}$ higher downward irradiance in the western leg compared to the eastern location. This bias has been considered/adjusted for the cloud-free observations and simulations and does not affect the comparison in Figure 2b.

The observed $F^{\downarrow}_{\mathrm{sw,cf}}$ is 8.8 $\mathrm{W{\cdot}m^{-2}}$ lower than the simulations using the cloud-free thermodynamic profile. A reasonable source for this significant difference, besides uncertainties in observations and simulations, is the neglect of aerosol extinction in the simulations. During the flight, manual observations reported a particularly hazy atmosphere. Using radiative transfer simulation with the aerosol type maritime clean (Hess et al., 1998), an optical thickness equivalent of 0.065 for this situation was estimated to match the observations. Thus, the measurement-based approach includes the aerosol/haze direct radiative effect in the cloud-free reference $F^{\downarrow}_{\mathrm{sw,cf}}$, which is excluded by the radiative transfer-based approach by simulating only the cloud-free and aerosol-free atmosphere.

The impact of the changing thermodynamic profile data between the cloudy and cloud-free atmosphere on the simulated cloud-free reference value of downward shortwave irradiances has been estimated by comparing the simulated $F^{\downarrow}_{\mathrm{sw,cf}}$ for the cloud-free thermodynamic profile data (Figure 1b blue hatched) with the one using the thermodynamic profile of the cloudy atmosphere without a cloud and the same SZA (Figure 1b gray). On average, the cloud-free reference $F^{\downarrow}_{\mathrm{sw,cf}}$ was 3.6 $\mathrm{W{\cdot}m^{-2}}$ lower when simulated for the thermodynamic profile of the cloudy atmosphere without a cloud, representing the radiative transfer-based approach, compared to the drier cloud-free thermodynamic profile (Figure 1b) theoretically observed by the measurement-based approach (aerosol-free atmosphere).

The simulated $F^{\downarrow}_{\mathrm{sw,cf}}$ is also affected by the assumed surface albedo due to multiple reflection between surface and atmosphere. As shown in Figure 2a, the surface albedo of the cloudy and cloud-free case differs. Simulations using these two surface albedo values to estimate $F^{\downarrow}_{\mathrm{sw,cf}}$ differ by 0.8 $\mathrm{W\ m^{-2}}$ in this particular case. Thus, the radiative transfer-based approach has the tendency to a slightly higher cloud-free reference $F^{\downarrow}_{\mathrm{sw,cf}}$ by applying the higher surface albedo observed in cloudy conditions compared to values obtained by applying a lower cloud-free albedo. In conditions with optically thicker clouds and a larger snow grain size, potentially increasing the surface albedo by more than 0.1 compared to cloud-free conditions, this effect becomes more relevant.

#### 3.2.2. Longwave

In the evolving cloud-free area east of the cloud edge, the surface temperature slowly decreased from about −13°C below the clouds to −20°C at the cloud-free eastern end of the flight leg (Figure 1a). Consequently, the upward longwave irradiance (Figure 2c) in the evolving cloud-free state decreased from, on average, 255 $\mathrm{W{\cdot}m^{-2}}$ below the cloud field to 231 $\mathrm{W{\cdot}m^{-2}}$ (fluctuating between 225 and 240 $\mathrm{W{\cdot}m^{-2}}$) in cloud-free

conditions in the easterly section. The downward longwave irradiance measured or simulated for cloud-free conditions is influenced by the thermodynamic profile of the atmosphere and the aerosol load. The respective histograms of $F^{\downarrow}_{\mathrm{lw,cf}}$ are shown in Figure 2c and reveal stronger fluctuations for the observed longwave downward irradiance in the cloud-free area (blue) than the simulated one based the atmospheric profiles observed in the cloud-free region (blue hatched). While the simulations are based on a local atmosphere profile, the inhomogeneous conditions in the MIZ caused by leads and nilas, result in a broader range of the boundary layer thermodynamics (Tetzlaff et al., 2015), which broadens the distribution of observed downward longwave irradiance.

The simulated $F^{\downarrow}_{\mathrm{lw,cf}}$ in the cloud-free area indicates a 3 $\mathrm{W{\cdot}m^{-2}}$ lower downward irradiance compared to the observations, which again suggests the presence of aerosol or haze particles (not included in the simulations). Ritter et al. (2005) reported a similar range of longwave radiative effects due to aerosol layers.

The changes of the thermodynamic profile in cloudy and cloud-free conditions are substantial as clouds significantly influence the temperature and humidity profile. Below the cloud-field a warmer near-surface air temperature and cloud top temperature inversion as well as a higher specific humidity (Figure 1b) induce a 8 $\mathrm{W{\cdot}m^{-2}}$ higher $F^{\downarrow}_{\mathrm{lw,cf}}$ (reference value of the radiative transfer-based approach) compared to the cloud-free atmosphere in the east (Figure 2c; Table 1).

### 3.3. Impact of the Cloud-Free Reference on the CRF

#### 3.3.1. Shortwave CRF

The derived values of the shortwave CRF resulting from both approaches are illustrated in Figure 2d. By using the atmospheric thermodynamic profile data and the surface albedo (both measured in cloudy conditions) for simulating the reference cloud-free case, a weak shortwave cooling effect of −15 $\mathrm{W{\cdot}m^{-2}}$ is obtained for the radiative transfer-based CRF. This value is mostly caused by the high snow albedo in cloudy conditions (0.874), which reduces the potential shortwave cooling effect by the cloud. The measurement-based CRF is calculated exclusively from observations by subtracting the net irradiances observed below the cloud from the corresponding observations in the cloud-free area. In this measurement-based approach, the cooling effect of the cloud is stronger by about two thirds and amounts to −25 $\mathrm{W{\cdot}m^{-2}}$. This observed difference between both approaches is in the range reported by (Stapf et al., 2020a) derived using radiative transfer simulations.

The comparison between observed and radiative transfer-simulated irradiances (Section 3.2.1) enables the quantification of the differences between the two CRF approaches caused by changes in the atmospheric humidity, the potential hazy conditions, and in simulated surface albedo. The measurement-based CRF underestimates the shortwave CRF by 1.4 $\mathrm{W{\cdot}m^{-2}}$ due to the haze radiative effect included in the cloud-free reference. Also the radiative transfer-based CRF underestimates the cooling effect of the clouds by 0.6 $\mathrm{W{\cdot}m^{-2}}$ by neglecting the effects of the atmospheric humidity changes on the cloud-free reference. Due to the slightly overestimated multiple scattering in the cloud-free atmosphere using the higher surface albedo in cloudy conditions as input for the simulations of $F^{\downarrow}_{\mathrm{sw,cf}}$, the radiative transfer-based CRF overestimates the cooling effect of the clouds by 0.1 $\mathrm{W{\cdot}m^{-2}}$. Thus, in this case study both approaches slightly underestimate the cloud-free reference net irradiances. Nevertheless, the strongest contribution to the difference between both CRF approaches is induced by the changing snow albedo in both states (10.5 $\mathrm{W{\cdot}m^{-2}}$). Differences caused by the atmospheric thermodynamic properties or multiple scattering appear minor.

To reduce this significant albedo-induced difference for the radiative transfer-based CRF, a surface albedo estimate representing cloud-free conditions obtained from observations below clouds is required to improve the cloud-free reference. The cloud-free albedo retrieved from the observations below the cloud ($\alpha_{\mathrm{cf,ret}}$) shown in Figure 2a (red) agrees roughly with the true surface albedo in cloud-free conditions. Nevertheless, this slight underestimation of the cloud-free surface albedo needs to be considered in the interpretation of the radiative transfer-based shortwave CRF using the biased cloud-free albedo retrieval as shown in Figure 2d (red). An overestimate of the shortwave cooling by 2.8 $\mathrm{W{\cdot}m^{-2}}$ for the improved radiative

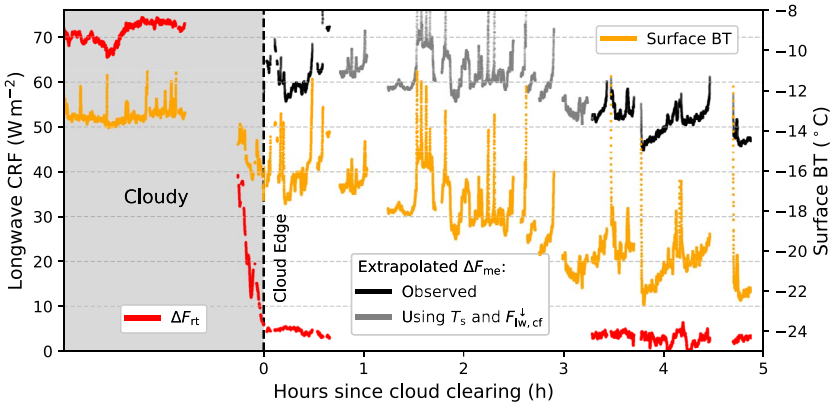


**Figure 3.** West-east cross-section of the observed cloud edge scene shown in Figure 1. The time-axis represents the hours after dissolution of cloud-field (gray area) estimated from the cloud edge position derived from earlier satellite observations (red dashed lines in Figure 1). The local radiative transfer-based longwave CRF for the low-level sections is shown in red, the surface BT for all altitudes below clouds in orange. Leads and nilas are excluded. Measurements recorded in the cloudy scene taken in combination with running values observed in the cloud-free area, as a cloud-free reference, illustrate the evolution of the measurement-based longwave CRF (black and gray). Please note that the real CRF cancels in the cloud-free area, as indicated by the radiative transfer-based longwave CRF.

transfer-based shortwave CRF using $\alpha_{cf,\,ret}$ ($-28$ W·m$^{-2}$) compared to the measurement-based approach illustrates the sensitivity of the shortwave CRF to the slightly biased cloud-free albedo estimate. However, it should be stressed that areal surface albedo observations obtained over large areas might not represent local radiative transfer effects in the heterogeneous Arctic environment (Figure 1a), whereby also the observations and the cloud-free surface albedo estimate may cause significant uncertainties. Taking these circumstances into account, this improved shortwave CRF approach provides a promising solution to close the gap between measurement-based and radiative transfer-based approach and realistically and continuously represent the cloud-free reference of shortwave net irradiances.

### 3.3.2. Longwave CRF

The longwave CRF estimated from both approaches are shown in Figure 2e. While the measurement-based CRF amounts to 51 W·m$^{-2}$ on average, the radiative transfer-based CRF provides a significantly stronger warming by the clouds (71 W·m$^{-2}$). Even if the cloud-free longwave bias (haze, aerosol effect) is substracted from the longwave net irradiances of the measurement-based CRF a 16 W·m$^{-2}$ weaker warming effect is found compared to the radiative transfer-based CRF. Thus, relevant for the cloud-free reference irradiances of both approaches discussed in Section 3.2.2, the change to a colder cloud-free surface temperature (equivalent of 24 W·m$^{-2}$ of upward irradiance, Table 1) clearly dominates over changes induced by the slightly colder and drier atmosphere in the cloud-free area (8 W·m$^{-2}$ of downward irradiance estimated from $F^{\downarrow}_{lw,rt}$ neglecting the haze, aerosol effect, Table 1).

The surface temperature adaption to the new cloud-free environment (Figure 1a) suggests a strong temporal dependence of the longwave net irradiances used as a reference for the measurement-based CRF. By using the cloud edge positions estimated from satellite images (Figure 1, red dashed), for each location of the flight track in the cloud-free area, a rough estimate of the time elapsed after the cloud-field dissolved was estimated. The resulting temporal evolution of the measurement-based longwave CRF is shown in Figure 3 extrapolated into the cloud-free area, from where the required reference values originate from. These values are deliberately shown contradictory in the cloud-free area, where the CRF (red line, radiative transfer-based CRF) actually vanishes. However, the extrapolated measurement-based longwave CRF have been calculated using the mean longwave net irradiance observed below the cloud (fixed value, excluding the edge) in combination with the cloud-free reference irradiances (running values), based on the choice of the cloud-free atmosphere and surface temperature reference observed in the cloud-free area at a certain time after dissolution of cloud-field. Due to the flight pattern, low-level observations of the cloud-free reference

(black) are available in the first hour and from 3 to 5 h after the clearing. To fill this gap (gray line), the upward irradiance was estimated from the measured surface temperature (assuming a surface emissivity of 0.99) and the downward irradiance is used from the cloud-free simulations (output for surface levels).

The decrease of the surface temperature (Figure 3 orange) already starts below the cloud-field (gray shaded area) toward the cloud edge. With the thinning of the cloud-field toward the cloud edge, also the longwave warming of the cloud (red line) is significantly reduced and leads to a slight cooling of the surface temperature of 2.5 K. As a consequence, already for the freshly cloud-free environment (average of the first kilometer) the measurement-based and radiative transfer-based CRF differ (cloud-edge excluded). The measurement-based CRF amounts to 62 $W{\cdot}m^{-2}$ (Figure 3, black), which is already 9 $W{\cdot}m^{-2}$ weaker compared to the radiative transfer-based approach (71 $W{\cdot}m^{-2}$). In the evolving cloud-free area, the reference longwave net irradiance strongly fluctuates due to surface temperature heterogeneities (excluding leads and nilas), but the minima of the surface temperature steadily decrease. However, the measurement-based CRF stays roughly constant for the first 2.5 h because the upward and downward irradiance decrease with a similar rate. After this time span, the surface cooling exceeds the atmospheric changes and the longwave net irradiance became less negative. Using cloud-free observations with more than 3 h delay after dissolution of the cloud field (eastern end of the flight leg) results in the longwave measurement-based CRF of around 50 $W{\cdot}m^{-2}$ shown in Figure 2. If the new cloud-free state was fully established cannot be conclusively determined by these observation as the full surface energy budget components are not available and also advection-induced thermodynamic changes cannot be excluded.

#### 3.3.3. Total (Shortwave Plus Longwave) CRF

The total CRF calculated from the different approaches is shown in Figure 2f. The radiative transfer-based approach quantifies a total warming effect of 55 $W{\cdot}m^{-2}$, while the measurement-based technique reveals a warming effect of 27 $W{\cdot}m^{-2}$. This comparison clearly demonstrates how significant the quantitative differences in CRF estimates are. With the help of a continuous cloud-free albedo retrieval, the radiative transfer-based shortwave CRF corresponds more closely to the measurement-based CRF. This total radiative transfer-based CRF using the cloud-free albedo retrieval results in 42 $W{\cdot}m^{-2}$.

The case study analyzed here, follows the transition from cloudy to cloud-free conditions. The opposite scenario, where a cloud field moves into a cloud free area will be different. The thermodynamic state in the cloudy environment will change over time while the cloud-free reference for the longwave measurement-based CRF would be fixed. A high temporal resolution of thermodynamic state observations will be key to understand this transition. Starting with similar longwave CRF estimates of both approaches, the results will diverge over time until the new thermodynamic equilibrium in the cloudy state is reached.

Although these results represent a single case study only, we conclude that the temporal dependence of the cloud-free reference needs to be considered when calculating the measurement-based CRF.

## 4. Influence of Thermodynamic State Changes on the Longwave Cloud-Free Reference and CRF During SHEBA

The difference between the measurement-based and radiative transfer-based longwave CRF strongly depends on the thermodynamic profiles and the surface temperatures, which are subject to significant changes over the course of a year. To estimate the differences between both approaches for a full annual cycle in the Arctic, SHEBA radiosoundings (Moritz, 2017) with a temporal resolution between 6 and 12 h were analyzed. Based on ground-based cloud-fraction observations (Persson, 2011), these profiles are separated in soundings representing overcast (cloud-fraction above 95%) or mostly cloud-free conditions where, at least during one time-step during the timespan of the sounding, a cloud fraction below 10% was indicated. The analysis was limited to cases with a cloud base height below 4 km (remote sensing data from Shupe et al. (2007) were used), where the clouds have a significant impact on the longwave REB (Shupe & Intrieri, 2004). This altitude threshold represents the upper limit of "opaquely cloudy" defined in Stramler et al. (2011). The advantage of filtering the clouds by altitude is that the preselection of atmospheric profiles is independent of the actual strength of the CRF and cloudy longwave net irradiances, which might change

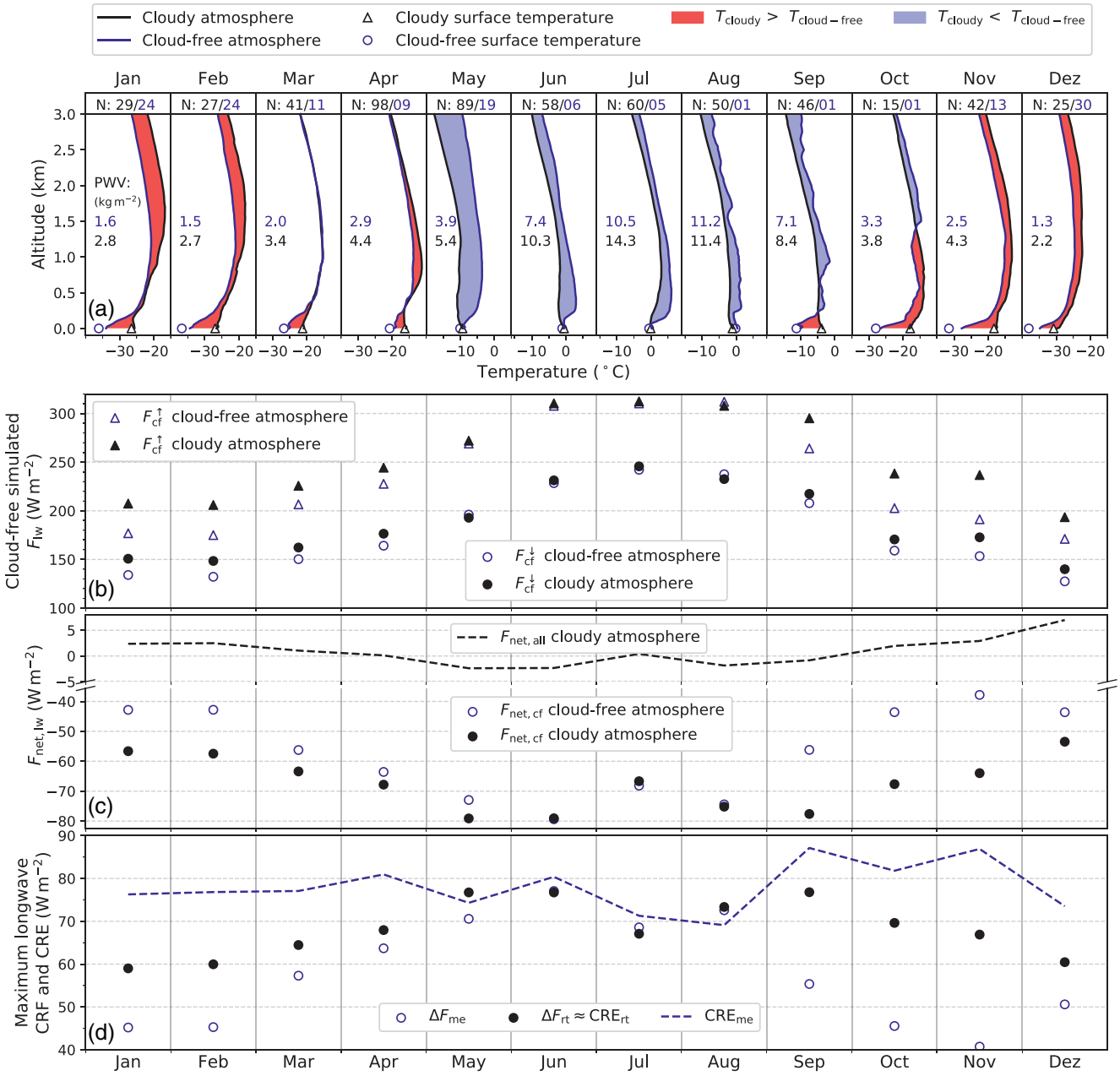


**Figure 4.** (a, upper row) Monthly mean SHEBA atmospheric temperature profiles for cloudy (black line) conditions (cloud-fraction above 95%) and cloud-free (blue line) conditions (cloud fraction below 10%). Blue/red shadings indicate a cooler/warmer cloudy atmosphere compared to the cloud-free atmosphere. Corresponding monthly mean surface temperatures are shown in open markers. Precipitable water vapor values integrated up to 500 hPa are given and the number of profiles (N) for cloudy (black) and cloud-free (blue) conditions on top of panel (a). Constant *x*-scale span (25 K). (b) Cloud-free upward and downward longwave irradiances simulated from the monthly cloudy or cloud-free thermodynamic profiles in (a). (c) Longwave net irradiances of the cloud-free reference estimated for both atmospheric profiles are shown in blue and black scatter points. Longwave net irradiances in the cloudy atmosphere with an optical thick boundary layer cloud are shown with a black dashed line. Please note the split *y*-axis and the changing scale. (d) CRF calculated for an optically thick boundary layer cloud in the cloudy atmosphere using either the radiative transfer-based approach $\Delta F_{rt}$ (cloudy atmosphere reference) or the measurement-based $\Delta F_{me}$ (cloud-free atmosphere reference). The CRE (only downward irradiances) for the measurement-based approach ($CRE_{me}$) is shown in a dashed blue line, the radiative transfer-based $CRE_{rt}$ is approximately represented by the $\Delta F_{rt}$ (difference < 1 W·m$^{-2}$).

during the year. The monthly averaged vertical profile data are shown in Figure 4a for the entire year of the SHEBA campaign. Similarly, the corresponding surface temperatures observed during each sounding were averaged. Due to the seasonal cycle of cloud-fraction during SHEBA (Intrieri et al., 2002) an equal number of cloudy and cloud-free profiles are available in winter, however, from August to October cloud-free states

are rare and the representativeness appears limited. Also the cloud-free periods in summer are less persistent and might influence the related atmospheric thermodynamic adjustment. However, these sampling issues represent and illustrate the nature of the observation-based approach.

Based on these data, the cloud-free longwave upward, downward (Figure 4b) and net irradiances (Figure 4c) were simulated for each month, either assuming the thermodynamic profiles of the cloudy or cloud-free state. Then, both simulated net irradiances assuming cloud-free conditions were used in combination with the net irradiances simulated in the cloudy atmosphere (assuming constant cloud properties) (Figure 4c) to estimate the CRF obtained by the radiative transfer-based and measurement-based approach (Figure 4d).

### 4.1. Longwave Irradiances for the Cloud-Free Reference

In the cold season (October to February), the surface temperature is around 10 K warmer under clouds compared to cloud-free conditions (Figure 4a). This spread slowly decreases toward the summer-time melting stage, where the surface temperature is fixed to the melting temperature of snow and ice and clouds have a small effect on the surface temperature. Consequently, the cloud-free upward longwave irradiances estimate from the radiative transfer-based approach (Figure 4b) is around 30–40 $W \cdot m^{-2}$ higher in autumn and winter compared to the measurement-based approach, while in summer almost identical values are calculated for both techniques.

For the downward longwave irradiances, a complex interaction between temperatures, atmospheric stability, and the water vapor content (precipitable water vapor, PWV) determines the specific monthly values. In general, the water vapor content increases toward the summer and is lower in the cloud-free atmosphere compared to cloudy conditions (PWV values are embedded in Figure 4a). Thus, the cloud-free state potentially emits less downward longwave radiation. However, while the cloudy atmosphere in winter is in general warmer compared to the cloud-free one (indicated by red shadings in Figure 4a), from May till August this relation is reversed (indicated by blue shadings) and compensates the humidity differences between both states in summer. As a result, the downward irradiances estimated from the radiative transfer-based approach are higher compared to cloud-free irradiances obtained with the measurement-based approach. This difference vanishes in the summer months although the cloud-free atmosphere appears significantly warmer during that season. During summer, similar near-surface air temperatures between both states and an increased PWV reduces the impact of the significantly warmer upper cloud-free atmosphere. In terms of absolute values, the change of the upward irradiance due to different surface temperatures in both atmospheric states (maximum 45 $W \cdot m^{-2}$) dominates over changes in the downward irradiances (maximum 20 $W \cdot m^{-2}$). Consequently, a difference between the cloud-free reference net longwave irradiances of both approaches is expected.

The combination of surface temperature and effective atmospheric BT determines the longwave net irradiances, whereby the latter is driven by the lapse rate, especially in low altitudes. As a measure of the lapse rate and the potential atmospheric stability the difference between surface temperature and maximum atmospheric temperature is used, which increases in both states toward the winter month. This difference peaks at 16 K (10 K) in cloud-free (cloudy) conditions; it represents one reason for less negative net irradiances in winter compared to summer. However, more important for the absolute change in net irradiance is the Planck radiation law, where the wavelength-integrated irradiance is proportional to the temperature to the power of four. The surface temperatures change from almost −40°C in cloud-free conditions in winter to values close to zero during the melting stage of sea ice and snow in the summertime Arctic. In addition, the BT difference between surface and atmosphere in cloud-free conditions is large, whereby the nonlinearity unfolds its effect (only small impact expected for cloudy net irradiances). Thus, assuming a hypothetical constant lapse rate scaled to warmer temperatures in summer, a more negative longwave net irradiance is found in cloud-free conditions during this season (similar principle of Planck radiative climate feedback). In the cold season, instead, a relatively warm atmosphere relative to the surface temperature will, in combination with the general low temperatures, cause significantly less negative (outgoing) net irradiances for the Arctic winter cloud-free state. Stramler et al. (2011) characterized the cloud-free mode during the SHEBA winter with values around −40 $W \cdot m^{-2}$. Radiative transfer simulations of the cloud-free net irradiances using the measured cloud-free atmosphere in Figure 4c (blue scatter points), indicate similar values in winter.

In summer, however, the cloud-free mode should occur between −70 and −80 W·m$^{-2}$, which highlights the potential seasonal variability in longwave modes structures, which are relevant for the measurement-based CRF.

Combining upward and downward irradiances, in nonsummer months, the longwave cloud-free net irradiances obtained from the radiative transfer-based approach (Figure 4c, black scatter points) are systematically more negative (outgoing) compared to the measurement-based approach (Figure 4c, blue scatter points) under cloud-free conditions. This difference peaks at almost 25 W·m$^{-2}$ in late autumn (10–15 W·m$^{-2}$ in winter) and vanishes in summer. The longwave cloud-free net irradiance derived from the radiative transfer-based approach in winter indicates values around −55 W·m$^{-2}$. In the cloud-free atmosphere these values rarely occur (Stramler et al., 2011) as a consequence of thermodynamic state changes.

### 4.2. Influence on CRF

To estimate measurement-based and radiative transfer-based CRF, a fixed opaque low-level cloud (cloud extent from 50–250 m altitude, LWP 100 g·m$^{-2}$) was assumed to simulate the irradiances of the cloudy state shown in Figure 4c (black dashed line). Because cloud properties in the Arctic are highly variable, we have assumed a rather thick and low cloud to analyze the maximum (saturated) effect on the downward irradiance, and to interpret the entire annual cycle independent of the seasonal variability of cloud fraction and liquid/ice water content. Due to the low and opaque character of the cloud, the cloudy net irradiances are close to zero. From May to September the net irradiances tend to be slightly negative due to the more neutral atmospheric lapse rate in low altitudes. Toward the winter, the rather stable conditions (also during the cloudy state) cause slightly positive cloudy net irradiances, which are commonly observed in the cloudy winter mode (Stramler et al., 2011). Thus, the tendency of more negative longwave irradiances toward the summer is similar to the cloud-free net irradiances, which reduces the spread between the cloudy and cloud-free longwave net irradiances, the CRF, in all seasons. Calculated from the net irradiances in Figure 4c, the monthly mean CRF for both approaches is shown in Figure 4d (scatter points, left *y*-axis).

In summer, the CRF derived from both approaches is almost similar fluctuating between 68 and 78 W·m$^{-2}$. In July a significant decrease in both longwave CRF estimates is obvious. This feature is caused by the warmest and most humid atmosphere state of the entire year, while the surface temperature is similar to other summer month. Cox et al. (2015) showed that with increasing PWV and fixed temperature, the longwave CRF decreases. This results in the highest cloud-free downward irradiance of the year (Figure 4b) and highlights the importance of the thermodynamic profile parameters to estimate the CRF. As the thermodynamic profiles significantly change in the course of the year and, thereby, influences the maximum longwave CRF, the atmospheric background needs to be considered, when the CRF is analyzed as a function of cloud liquid or total water path.

In the cold season the difference between the CRF estimates increases toward the bias induced by the difference in cloud-free net irradiances, and thus, results in a systematically higher longwave CRF estimated by the radiative transfer-based approach compared to the measurement-based CRF. The difference between both approaches peaks in autumn, as the atmosphere in the cloudy state is still relatively warm compared to the surface in cloud-free conditions, which already strongly cools. Thus, the weakest warming effect of clouds occurs in late autumn (measurement-based CRF), while the radiative transfer-based CRF does not account for this feature and indicates the weakest warming effect of clouds in winter. This suggests, that the longwave CRF estimates of both approaches is not only offset, but also the seasonal cycle of the obtained CRF might be shifted. While in winter the measurement-based CRF is limited by the differences within the two Arctic winter modes of longwave net irradiance (40 W·m$^{-2}$) (Stramler et al., 2011), the radiative transfer-based CRF reaches values around 60 W·m$^{-2}$ in winter. Comparing the annual mean CRF, the measurement-based CRF clearly suggests a weaker maximum impact of clouds (58 W·m$^{-2}$) compared to the radiative transfer-based CRF, which amounts to 68 W·m$^{-2}$.

Looking only at the downward components, the CRE (Figure 4d), clouds tend to increase the downward irradiance around the year on average by 78 W·m$^{-2}$ compared to the real cloud-free atmosphere (measurement-based CRE, dashed blue line) with a peak in autumn. The radiative transfer-based CRE is approximately equal to the radiative transfer-based CRF due to a small contribution (<1 W·m$^{-2}$) of the downward

longwave irradiance reflected by the surface (Stapf et al., 2020a). Using the radiative transfer-based approach (black scatter points), clouds only increase the downward longwave irradiance by 69 $W \cdot m^{-2}$ (strongest from May to September). Thus, in contrast to the CRF differences estimated by both approaches, the radiative transfer-based CRE suggest a weaker warming effect than the measurement-based CRE, which highlights a required careful interpretation of the observed quantity.

Although the CRF indicates the strongest warming effect in summer, the relative contribution of clouds to the downward irradiance in cloudy conditions estimated from the ratio of longwave radiative transfer-based CRE and the downward longwave irradiance in the cloudy atmospheric profile simulated cloud-free (radiative transfer-based CRE / $F_{cf}^{\downarrow}\big|_{rt}$) is weakest in the summer months with 31%, compared to an average 40% in all other months. This relative measure of the contribution by clouds to the downward irradiance in cloudy conditions might represent an interesting alternative to separate the cloud impact from the atmospheric background. In other words, clouds in winter are more impactful and their presence causes a stronger relative enhancement of downward irradiance in the cloudy atmosphere compared to summer.

## 5. Conclusion

Different concepts to derive the CRF have been applied in the past to study the warming or cooling effect of clouds in the Arctic. One group of techniques is based on radiative transfer simulations to derive the net irradiances under cloud-free conditions. In this approach, the thermodynamic vertical profile is obtained from measurements in the cloudy state, which is applied to simulate the reference irradiances in theoretically assumed cloud-free conditions. A second approach is based on measurements of irradiances only, which are clearly separated into observations in both the cloudy and the cloud-free cases.

Based on the methodology and definition of both approaches, we conclude that it is important to carefully consider the differences between both approaches. The radiative transfer-based approach represents an instantaneous measure of CRF relative to a cloudy thermodynamic atmospheric background, while the measurement-based approach describes the impact of the presence of clouds on the surface energy budget accounting for related state changes of the thermodynamic atmospheric properties between cloudy and cloud-free conditions.

The measurement-based CRF definition aims to quantify the development of the surface energy budget (not only radiative), influenced by the presence or absence of clouds, as the result of an interplay between radiative, turbulent, and conductive fluxes in the Arctic. The transition from a cloudy atmospheric thermodynamic profile into a new cloud-free equilibrium state, and vice versa (cloud-free into cloudy), is time-dependent. Such temporal adaptions are not addressed by the definition of the CRF after Ramanathan et al. (1989), but are evidently included in the CRF derived from observations only. The radiative transfer-based CRF does not account for this response of the energy budget and thermodynamic adjustment of the atmosphere, it rather represents an instantaneous forcing to preserve the prevailing REB.

To discuss the systematic differences and the representativeness of both CRF estimates, a case study from the AFLUX campaign with a sharp and distinct cloud edge separating a cloudy boundary layer from an evolving cloud-free state was analyzed. To extend this case study to different seasons, both longwave CRF estimates were simulated using SHEBA data covering a full annual cycle. By a comparison of the CRF estimates, we conclude:

1. The shortwave radiative transfer-based CRF indicates a weaker cooling effect of clouds compared to the measurement-based CRF, mainly due to the difference between cloudy and cloud-free snow albedo (atmospheric property changes have a minor impact). The observed differences agree with estimates by Stapf et al. (2020a), which were based on simulations only
2. The longwave radiative transfer-based CRF provides a stronger warming effect of clouds compared to the measurement-based CRF by not accounting for the transition of the cloudy thermodynamic profile properties into a new cloud-free equilibrium state or vice versa (cloud-free into cloudy). Thereby, changes of the surface temperature (upward irradiance) between both states dominate over atmospheric thermodynamic changes (downward irradiance)

3. The annual cycle of longwave CRF from both approaches reveal significant differences (up to 25 $W \cdot m^{-2}$), except for the summer months due to surface melting and related fixed surface temperatures
4. The seasonal characteristic of atmospheric profiles of thermodynamic properties is a crucial driver of the CRF and important for the interpretation of the longwave CRF similar to cloud properties such as cloud fraction or liquid water path

The magnitude of the reported differences between both approaches to derive the longwave CRF hold only for the analyzed region and conditions during AFLUX and SHEBA. However, the described effects appear systematic and should be representative for similar conditions in the sea ice covered inner Arctic. Therefore, it is recommended to consider the thermodynamic influence on the CRF estimates in past, present, and future CRF studies, especially when the CRF of the different approaches are compared. Otherwise, such comparisons might become misleading.

Despite the systematic differences, there is no true or false choice between both CRF estimates. Both approaches serve different scientific purposes and may complement each other. While the radiative transfer-based CRF estimate does not predict the REB in the cloud-free state, it is most useful, if the instantaneous forcing values to preserve the prevailing REB are directly related to the atmospheric radiative background information. For example, the radiative transfer-based approach can be valuable to highlight the influence of an extraordinary warm and moist atmosphere during a warm air intrusion event relative to a climatological average profile, and to separate the impact of a new atmosphere (which can be significant, Yamanouchi, 2019) from advection-induced changes in cloud microphysical and macrophysical properties. However, relevant for the shortwave radiative transfer-based CRF, the interaction between the surface-albedo-cloud interaction (Stapf et al., 2020a) is an instantaneous effect, which is continuously adjusting the surface albedo and shortwave net irradiances to the prevailing cloud and illumination conditions. Thus, if the radiative transfer-based CRF is used to quantify the instantaneous impact of clouds on the REB, a continuous estimate of the unobserved surface albedo in cloud-free conditions is required, instead of using the observed cloudy albedo in the radiative transfer simulations.

For the measurement-based approach, the required cloud-free reference values are hard to obtain especially during longer cloudy periods. However, a statistical analysis of longwave net irradiances in both states obtained for certain locations and seasons enables to characterize mode structures, which gives some evidence about the states of the REB influenced by the presence of clouds. Thus, the measurement-based CRF is rather powerful to explain how the presence of clouds shapes the surface energy budget in the Arctic for a specific region and time of the year. The influence of the seasonal atmospheric profiles of thermodynamic properties on the REB and the CRF highlights the need for a proper representation of radiative mode structures, associated thermodynamic profiles, and state changes to realistically represent the CRF and cloud radiative feedback mechanisms in climate models.

Based on these different interpretations of the two CRF approaches, the mostly warming effect of Arctic clouds as often reported in literature needs to be considered as a result of an instantaneous radiative transfer-based measure of CRF. By accounting for processes like the surface-albedo-cloud interaction (Stapf et al., 2020a), which causes an increase of shortwave cooling effect of clouds above snow surfaces, as well as surface energy budget adjustments with consequences for the atmospheric thermodynamics, this general conclusion of mostly warming Arctic clouds might need to be rediscussed. Therefore, it is recommended to consider the specific use and interpretation of the CRF definitions for studies of the radiative effects of Arctic clouds.

## Data Availability Statement

Data were provided by NCAR/EOL under the sponsorship of the National Science Foundation (https://data.eol.ucar.edu/). The authors declare that they have no conflict of interest. The April 11, 2019 case study data (Stapf et al., 2020b) represent a subset of the entire AFLUX data set. This subset can be retrieved from the PANGAEA database (https://doi.pangaea.de/10.1594/PANGAEA.922184). The radiosoundings from Ny-Ålesund are available from Maturilli (2020). SHEBA data are used from Shupe et al. (2007), Persson (2011), and Moritz (2017).

**Acknowledgments**
The authors thank the two anonymous reviewers for their constructive comments to improve this study. We gratefully acknowledge the funding by the Deutsche Forschungsgemeinschaft (DFG, German Research Foundation)—Project Number 268020496—TRR 172, within the Transregional Collaborative Research Center "ArctiC Amplification: Climate Relevant Atmospheric and SurfaCe Processes, and Feedback Mechanisms (AC)[3]." The authors are grateful to AWI for providing and operating the Polar 5 aircraft during the AFLUX campaign. We thank the crew of Polar 5 and the technicians of the aircraft for excellent technical and logistical support. The generous funding of the flight hours for AFLUX by AWI is greatly appreciated. We thank Jörg Hartmann and Christof Lüpkes (Alfred Wegener Institute, Helmholtz Centre for Polar and Marine Research, Bremerhaven) for providing AFLUX in situ meteorological data. We thank Kerstin Ebell (University of Cologne) for useful comments to this manuscript. Open access funding enabled and organized by Projekt DEAL.

## References

Allan, R. P., & Ringer, M. A. (2003). Inconsistencies between satellite estimates of longwave cloud forcing and dynamical fields from reanalyses. *Geophysical Research Letters*, *30*(9), 1491. https://doi.org/10.1029/2003GL017019

Cox, C. J., Uttal, T., Long, C. N., Shupe, M. D., Stone, R. S., & Starkweather, S. (2016). The role of springtime Arctic clouds in determining autumn sea ice extent. *Journal of Climate*, *29*(18), 6581–6596. https://doi.org/10.1175/JCLI-D-16-0136.1

Cox, C. J., Walden, V. P., Rowe, P. M., & Shupe, M. D. (2015). Humidity trends imply increased sensitivity to clouds in a warming Arctic. *Nature Communications*, *6*(1), 10117. https://doi.org/10.1038/ncomms10117

Dong, X. Q., Xi, B. K., Crosby, K., Long, C. N., Stone, R. S., & Shupe, M. D. (2010). A 10 year climatology of Arctic cloud fraction and radiative forcing at Barrow, Alaska. *Journal of Geophysical Research*, *115*(D17), D17212. https://doi.org/10.1029/2009JD013489

Ebell, K., Nomokonova, T., Maturilli, M., & Ritter, C. (2020). Radiative effect of clouds at Ny-Ålesund, Svalbard, as inferred from ground-based remote sensing observations. *Journal of Applied Meteorology*, *59*(1), 3–22. https://doi.org/10.1175/JAMC-D-19-0080.1

Ehrlich, A., Wendisch, M., Lüpkes, C., Buschmann, M., Bozem, H., Chechin, D., et al. (2019). A comprehensive in situ and remote sensing data set from the Arctic CLoud Observations Using airborne measurements during polar Day (ACLOUD) campaign. *Earth System Science Data*, *11*(4), 1853–1881. https://doi.org/10.5194/essd-11-1853-2019

Emde, C., Buras-Schnell, R., Kylling, A., Mayer, B., Gasteiger, J., Hamann, U., et al. (2016). The libradtran software package for radiative transfer calculations (version 2.0.1). *Geoscientific Model Development*, *9*(5), 1647–1672. https://doi.org/10.5194/gmd-9-1647-2016

Gardner, A. S., & Sharp, M. J. (2010). A review of snow and ice albedo and the development of a new physically based broadband albedo parameterization. *Journal of Geophysical Research*, *115*(F1), F01009. https://doi.org/10.1029/2009JF001444

Graham, R. M., Rinke, A., Cohen, L., Hudson, S. R., Walden, V. P., Granskog, M. A., et al. (2017). A comparison of the two Arctic atmospheric winter states observed during N-ICE2015 and SHEBA. *Journal of Geophysical Research*, *122*(11), 5716–5737. https://doi.org/10.1002/2016JD025475

Hess, M., Koepke, P., & Schult, I. (1998). Optical properties of aerosols and clouds: the software package OPAC. *Bulletin of the American Meteorological Society*, *79*(5), 831–844.

Intrieri, J. M., Fairall, C. W., Shupe, M. D., Persson, P. O. G., Andreas, E. L., Guest, P. S., & Moritz, R. E. (2002). An annual cycle of Arctic surface cloud forcing at SHEBA. *Journal of Geophysical Research*, *107*(C10), 8039. https://doi.org/10.1029/2000JC000439

Maturilli, M. (2020). *High resolution radiosonde measurements from station Ny-Ålesund (2017-04 et seq)*. Alfred Wegener Institute - Research Unit Potsdam, PANGAEA. https://doi.org/10.1594/PANGAEA.914973

Miller, N. B., Shupe, M. D., Cox, C. J., Noone, D., Persson, P. O. G., & Steffen, K. (2017). Surface energy budget responses to radiative forcing at Summit, Greenland. *Cryosphere*, *11*(1), 497–516. https://doi.org/10.5194/tc-11-497-2017

Miller, N. B., Shupe, M. D., Cox, C. J., Walden, V. P., Turner, D. D., & Steffen, K. (2015). Cloud radiative forcing at Summit, Greenland. *Journal of Climate*, *28*(15), 6267–6280. https://doi.org/10.1175/JCLI-D-15-0076.1

Moritz, R. (2017). *Soundings, Ice Camp NCAR/GLAS raobs. (ASCII). Version 2.0*. UCAR/NCAR - Earth Observing Laboratory. https://doi.org/10.5065/D6FQ9V0Z

Perovich, D. K., Grenfell, T. C., Light, B., & Hobbs, P. V. (2002). Seasonal evolution of the albedo of multiyear Arctic sea ice. *Journal of Geophysical Research*, *107*(C10). https://doi.org/10.1029/2000JC000438

Persson, P. O. G. (2011). *SHEBA composite data observations. Version 1.0*. UCAR/NCAR - Earth Observing Laboratory. https://doi.org/10.5065/D6PN93R6

Persson, P. O. G., Fairall, C. W., Andreas, E. L., Guest, P. S., & Perovich, D. K. (2002). Measurements near the Atmospheric Surface Flux Group tower at SHEBA: Near-surface conditions and surface energy budget. *Journal of Geophysical Research*, *107*(C10). SHE 21-1–SHE 21-35. https://doi.org/10.1029/2000JC000705

Persson, P. O. G., Shupe, M. D., Perovich, D., & Solomon, A. (2017). Linking atmospheric synoptic transport, cloud phase, surface energy fluxes, and sea-ice growth: Observations of midwinter SHEBA conditions. *Climate Dynamics*, *49*(4), 1341–1364. https://doi.org/10.1007/s00382-016-3383-1

Ramanathan, V. L., Cess, R. D., Harrison, E. F., Minnis, P., Barkstrom, B. R., Ahmad, E., & Hartmann, D. (1989). Cloud-radiative forcing and climate: Results from the Earth Radiation Budget Experiment. *Science*, *243*(4887), 57–63.

Ritter, C., Notholt, J., Fischer, J., & Rathke, C. (2005). Direct thermal radiative forcing of tropospheric aerosol in the Arctic measured by ground based infrared spectrometry. *Geophysical Research Letters*, *32*(23), L23816. https://doi.org/10.1029/2005GL024331

Sedlar, J., Tjernstrom, M., Mauritsen, T., Shupe, M. D., Brooks, I. M., Persson, P. O. G., et al. (2011). A transitioning Arctic surface energy budget: The impacts of solar zenith angle, surface albedo and cloud radiative forcing. *Climate Dynamics*, *37*(7–8), 1643–1660. https://doi.org/10.1007/s00382-010-0937-5

Shupe, M. D., & Intrieri, J. M. (2004). Cloud radiative forcing of the Arctic surface: The influence of cloud properties, surface albedo, and solar zenith angle. *Journal of Climate*, *17*(3), 616–628. https://doi.org/10.1175/1520-0442(2004)017<0616:CRFOTA>2.0.CO;2.

Shupe, M. D., Intrieri, J. M., & Uttal, T. (2007). *ETL Radar-Lidar 10-min Cloud Physical Properties. Version 1.0*. UCAR/NCAR - Earth Observing Laboratory. https://doi.org/10.5065/D6MS3R4G

Stapf, J., Ehrlich, A., Jäkel, E., Lüpkes, C., & Wendisch, M. (2020). Reassessment of shortwave surface cloud radiative forcing in the Arctic: Consideration of surface-albedo–cloud interactions. *Atmospheric Chemistry and Physics*, *20*(16), 9895–9914. https://doi.org/10.5194/acp-20-9895-2020

Stapf, J., Ehrlich, A., & Wendisch, M. (2020). *Radiative energy budget, cloud radiative forcing, LWP, and cloud-free albedo derived from airborne broadband irradiance observations during AFLUX flight on 11 April 2019 (subset)*. PANGAEA. Retrieved from https://doi.pangaea.de/10.1594/PANGAEA.922184

Stramler, K., Del Genio, A. D., & Rossow, W. B. (2011). Synoptically driven Arctic winter states. *Journal of Climate*, *24*(6), 1747–1762. https://doi.org/10.1175/2010JCLI3817.1

Tetzlaff, A., Lüpkes, C., & Hartmann, J. (2015). Aircraft-based observations of atmospheric boundary-layer modification over Arctic leads. *Quarterly Journal of the Royal Meteorological Society*, *141*(692), 2839–2856. https://doi.org/10.1002/qj.2568

Tjernström, M., Shupe, M. D., Brooks, I. M., Achtert, P., Prytherch, J., & Sedlar, J. (2019). Arctic summer airmass transformation, surface inversions, and the surface energy budget. *Journal of Climate*, *32*(3), 769–789. https://doi.org/10.1175/JCLI-D-18-0216.1

Uttal, T., Curry, J. A., McPhee, M. G., Perovich, D. K., Moritz, R. E., Maslanik, J. A., et al. (2002). Surface heat budget of the Arctic Ocean. *Bulletin of the American Meteorological Society*, *83*(2), 255–275. https://doi.org/10.1175/1520-0477(2002)083⟨0255:SHBOTA⟩2.3.CO;2

Walden, V. P., Hudson, S. R., Cohen, L., Murphy, S. Y., & Granskog, M. A. (2017). Atmospheric components of the surface energy budget over young sea ice: Results from the N-ICE2015 campaign. *Journal of Geophysical Research*, *122*(16), 8427–8446. https://doi.org/10.1002/2016JD026091

Walsh, J. E., & Chapman, W. L. (1998). Arctic cloud-radiation-temperature associations in observational data and atmospheric reanalyses. *Journal of Climate*, *11*(11), 3030–3045. https://doi.org/10.1175/1520-0442(1998)011⟨3030:ACRTAI⟩2.0.CO;2

Warren, S. (1982). Optical properties of snow. *Reviews of Geophysics and Space Physics*, *20*(1), 67–89.

Wendisch, M., Macke, A., Ehrlich, A., Lüpkes, C., Mech, M., Chechin, D., et al. (2019). The Arctic cloud puzzle: Using ACLOUD/PASCAL multi-platform observations to unravel the role of clouds and aerosol particles in Arctic amplification. *Bulletin of the American Meteorological Society*, *100*(5), 841–871. https://doi.org/10.1175/BAMS-D-18-0072.1

Yamanouchi, T. (2019). Arctic warming by cloud radiation enhanced by moist air intrusion observed at Ny-Ålesund, Svalbard. *Polar Science*, *21*(SI), 110–116. https://doi.org/10.1016/j.polar.2018.10.009